Ocean Modelling 168 (2021) 101894

Contents lists available at ScienceDirect

Ocean Modelling

journal homepage: www.elsevier.com/locate/ocemod

The impact of surface currents on the wave climate in narrow fjords

Konstantinos Christakos [a,b,c,*], Jan-Victor Björkqvist [a,c,d], Øyvind Breivik [a,b], Laura Tuomi [c], Birgitte R. Furevik [a,b], Jon Albretsen [e]

[a] Norwegian Meteorological Institute, Allégaten 70, 5007 Bergen, Norway
[b] Geophysical Institute, University of Bergen, Allégaten 70, 5007 Bergen, Norway
[c] Finnish Meteorological Institute, Erik Palménin aukio 1, 00560 Helsinki, Finland
[d] Tallinn University of Technology, Department of Marine Systems, Akadeemia tee 15a, 12618 Tallinn, Estonia
[e] Institute of Marine Research, P.O. Box 1870, Nordnes, 5817 Bergen, Norway

ARTICLE INFO

Keywords:
Wind-waves
Current
Fjord
SWAN
ROMS
WRF

ABSTRACT

This study investigates the effect of surface currents on wind-generated waves in a complex coastal system with narrow fjords. The simulations are based on a phase-averaged wave model forced with surface currents from a high-resolution coastal ocean and fjord circulation model, and high-resolution winds from a nested atmospheric model. Wave simulations with and without ocean forcing are evaluated by comparing integrated wave parameters and modelled spectra with observations from five wave buoys. The comparison covers three winter seasons (2017–2020) and a case study. The wind sea part of the spectrum is better simulated at all locations when using the current forcing. At the most sheltered location, where wind sea dominated the wave climate, the wave height estimates improved by 12 percentage points when including current forcing. Spectral moments and the shape of the average spectra are also improved at most of the locations when current forcing is applied. The effect of wave–current interactions was found to be more pronounced at inner locations where the relative difference of spectral bandwidth is up 5%, the difference in directional spreading is greater than 5 degrees during strong surface currents, and the relative difference in peak frequency is exceeding 10%. Our results are consequential for narrow, deep and sheltered water bodies, but are not expected to carry over to shallow water areas.

1. Introduction

Predicting wave growth is essential for a range of oceanic and coastal applications, such as maritime transport, fish farming and ocean engineering. Nonetheless, the quality of wave predictions is highly affected by both atmospheric and ocean forcing. While the former generates wind waves, the latter modulates the existing wave field. The relative wind speed acting on the sea surface is modified by surface current, which in turn affects the wave growth. According to Ardhuin et al. (2012), the relative wind effect can explain about 20%–40% of the modulation in wave height induced by strong currents off the west coast of France. Surface currents also change the absolute wave frequency (f) through the Doppler shift. Spatial variation of surface currents modifies the relative wave frequency ($\sigma = 2\pi f - \boldsymbol{k} \cdot \boldsymbol{u}_c$, where $\boldsymbol{k}$ and $\boldsymbol{u}_c$ are the wavenumber and surface current vectors), and causes wave refraction and energy bunching/stretching.

Opposing currents can be associated with the occurrence of extreme wave heights, i.e., rogue waves (Onorato et al., 2011; Toffoli et al., 2015). Regions with strong wave–current interactions can enhance wave breaking (Melville et al., 2005; Romero et al., 2017). Romero et al. (2017) found large modulations of the wave height, up to 30%, due to wave–current interactions at the edge of an upwelling jet off the coast of Northern California and the Loop Current in the Gulf of Mexico. Their results showed large variations in wave breaking parameters, such as significant slope, whitecap coverage and directional spreading, with the two last ones being inversely correlated.

It is well known that large-scale wind-driven currents—such as the Gulf Stream (Mapp et al., 1985), the Kuroshio (Hwang, 2005) and the Agulhas current (Irvine and Tilley, 1988)—affect surface waves in the open ocean significantly. Ardhuin et al. (2017) found that also smaller scale currents (10–100 km) significantly affect ocean waves. Marechal and Ardhuin (2021) concluded that incident waves with small directional spreading (swell) experience stronger wave height gradients in the Agulhas region. Romero et al. (2020) found that, during low winds, the significant wave height in the Santa Barbara Channel can increase by up to 50%–80% in specific areas due to current-induced refraction. However, to our knowledge, the impact of currents on wind-generated waves in much narrower channels, e.g., fjords, has not been explored.

This study aims to quantify the impact of ocean currents on surface waves in fjords. Fjords are typically long, narrow and deep inlets of

* Corresponding author at: Norwegian Meteorological Institute, Allégaten 70, 5007 Bergen, Norway.
E-mail address: konstantinos.christakos@met.no (K. Christakos).

https://doi.org/10.1016/j.ocemod.2021.101894
Received 16 April 2021; Received in revised form 12 August 2021; Accepted 4 October 2021
Available online 12 October 2021

water. The water masses in fjords are often strongly stratified, containing three distinguishable water masses: (i) surface (brackish) water, (ii) intermediate water and (iii) basin (deep) water (e.g., Saetre, 2007). The surface layer often receives freshwater from rivers, but this is mixed with the more saline water flowing into the fjord from coastal and offshore regions, creating a brackish surface layer. The intermediate layer is located between the surface layer and the deep water, where the latter is typically bounded by the depth of the sill. The circulation in the intermediate layer is dominated by horizontal pressure gradients between coastal and fjord waters with longer time scales than upper layer dynamics. Tides affect the fjord dynamics at all levels.

The depth of the surface layer is about 1–10 m depending on the river runoff's strength (seasonal variation) and the amount of wind-driven mixing. The circulation in the surface layer is also strongly affected by winds and waves. The wave climate is mainly determined by the dominant wind direction and strength, the typical duration of low-pressure systems, and the geometry of the fjord system (fetch and width of fjords). As many Norwegian fjords are long with steep mountainsides, they are often exposed to intensified and topographically steered winds.

The Norwegian Coastal Current flows northwards along the Norwegian coast (Saetre, 2007). The current transports low salinity water from the Baltic Sea and the Norwegian rivers to the Barents Sea. It is primarily driven by density gradients (Garvine, 1995) and by the dominant southwesterly winds (Skagseth et al., 2011, and references herein).

In complex nearshore areas, such as the Norwegian coast, with thousands of islands and narrow channels, providing accurate wave forecasts is challenging. Two Norwegian organizations have developed and provide open-access operational wave forecasts along the Norwegian coast: (i) the Norwegian Meteorological Institute which provides coastal wave forecasts based on the WAM model (The Wamdi Group, 1988) with 800 m spatial resolution and (ii) the Norwegian Coastal Administration in cooperation with NORCE AS and BarentsWatch who have developed a coastal wave forecast system for fairways based on STWAVE (Massey et al., 2011) with 100 m spatial resolution (Furevik, 2017). None of these operational forecast systems accounts for the impact of surface currents on the waves in the coastal zone and in fjords. The imprint of currents on ocean waves in fjord areas has not been quantified, mainly due to a lack of appropriate high-resolution ocean forcing and observations. In these areas, remote sensing techniques, such as satellites, are not reliable (due to the land proximity), and the observations are mainly limited to point measurements such as wave buoys.

In 2016, the Norwegian Public Roads Administration (NPRA) launched one of the largest measurement campaigns of wind, wave and current conditions along the Norwegian coast. The Norwegian authorities aim to upgrade the coastal highway route, potentially replacing ferries on several fjord-crossings with bridges and tunnels. The measurement campaigns in the fjords provide the essential data for the design of these large state-of-the-art road projects but also function as advanced met-ocean studies in areas where they previously were not possible. This study has the overall goal of taking advantage of these unique measurements to improve our understanding of wave–current interactions for designing coastal structures, and aims at answering the following questions: (i) how important are the ocean currents for the wave modulation in a fjord system, (ii) which mechanisms affect the coastal and fjord waves, and (iii) what is the order of importance of current effects on waves in different fjord locations/conditions?

Our study is focused on a deep (more than 300 m deep in most places) fjord system located on the west coast of Norway (Fig. 1). Special attention is given to two areas: (i) Sulafjorden, equipped with buoys A–D, is a fjord exposed to strong swell from the Norwegian Sea, and (ii) the fjord cross-section near buoy F, as shown in Fig. 1.

This paper is organized as follows. Section 2 presents an overview of the wave model and the wave–current interaction theory, and Section 3 describes the results. Sections 4 and 5 discuss the results and present our conclusions.

2. Description of the modelling system

The study area is illustrated in Fig. 1 (also described in Christakos et al. (2020)). Buoys A, B, C, and D (Breisundet) are located in Sulafjorden, and buoy F is deployed at the junction between three fjords. Sulafjorden has an average width of 4–5 km and a length of about 10 km. Wind sea and swell conditions usually coexist in Sulafjorden due to its exposure to the open sea. However, the inner parts of the fjord system, e.g., location F, are characterized by a wave climate with only local wind sea and little or no swell.

2.1. The wave model

The wave model SWAN (Simulating WAves Nearshore, Booij et al., 1999; Ris et al., 1999) is a third-generation spectral model developed mainly for coastal applications. In this analysis, the SWAN cycle III version 41.20 is implemented for the fjord system. The model determines the evolution of the wave action density $N = E/\sigma$ (E is the wave variance density), dictated by the action balance equation

$$\frac{\partial N}{\partial t} + \frac{\partial (c_x N)}{\partial x} + \frac{\partial (c_y N)}{\partial y} + \frac{\partial (c_\sigma N)}{\partial \sigma} + \frac{\partial (c_\theta N)}{\partial \theta} = \frac{S_{total}}{\sigma}. \tag{1}$$

Here, c_x and c_y are the group velocity vector components in geographical (x, y)-space. The c_σ and c_θ represent the propagation in frequency–direction (σ, θ) space. The term S_{total} is defined in Eq. (2) as the sum of the individual source terms, where S_{in} is energy input generation by wind, S_{ds} is the dissipation induced by white-capping, S_{nl4} is the nonlinear wave energy transfer due to four-way wave (quadruplet) interactions, S_{nl3} is the three-way (triad) nonlinear interactions active in shallow to intermediate water, S_{fric} is the bottom friction and, S_{brk} is the depth-induced wave breaking,

$$S_{\text{total}} = S_{\text{in}} + S_{\text{ds}} + S_{\text{nl4}} + S_{\text{nl3}} + S_{\text{fric}} + S_{\text{brk}}. \tag{2}$$

S_{nl3} can be ignored in deep water and is switched off.

2.1.1. Saturation-based white-capping and wind input

We are using the saturation-based white-capping by Alves and Banner (2003), which is implemented in SWAN by van der Westhuysen et al. (2007). This white-capping parameterization is more accurate than the SWAN default by Komen et al. (1984) in mixed swell-wind sea conditions and was found to perform well in fjord areas in a previous study (Christakos et al., 2021). This white-capping function (S_{ds}) has two parts: a non-breaking part given by Komen et al. (1984) and a breaking part (S_{break}), which is defined as (SWAN team, 2017)

$$S_{\text{break}}(\sigma, \theta) = -C_{\text{ds}} \left(\frac{B(k)}{B_{\text{r}}} \right)^{p'/2} [\tanh(kd)]^{\frac{2-p_0}{4}} \sqrt{gk} E(\sigma, \theta). \tag{3}$$

Here, $C_{\text{ds}} = 0.50 \times 10^{-4}$ is the white-capping dissipation parameter, g is the acceleration due to gravity, and d is the water depth. The azimuthally integrated spectral saturation is given by $B(k) = E(\sigma)k^3 c_{\text{g}}$ where c_{g} is the wave group velocity. If $B(k)$ is under the threshold saturation level ($B_{\text{r}} = 1.75 \times 10^{-3}$) there is no wave breaking, but a background dissipation is obtained by $p' = 0$. If $B(k)$ is greater than B_{r}, there is breaking and $p' = p_0$ (p_0: a calibration exponent). Here, p' is given as a function of $B(k)$, in order to obtain a smooth change between these two conditions (Alves and Banner, 2003).

The wind input (S_{in}) is a combination of the formulations by Komen et al. (1984), Plant (1982), expressed by Yan (1987),

$$S_{\text{in}}(\sigma, \theta) = \left\{ \left[C_1 \left(\frac{u_*}{c} \right)^2 + C_2 \left(\frac{u_*}{c} \right) + C_3 \right] \cos(\theta - \theta_{\text{w}}) + C_4 \right\} \sigma E(\sigma, \theta). \tag{4}$$

where c is the phase velocity, θ_w is the wind direction, and C_{1-4} are coefficients (given by SWAN team (2017)). The friction velocity (u_*) estimate is based on Zijlema et al. (2012). The package will hereafter be denoted WESTH.

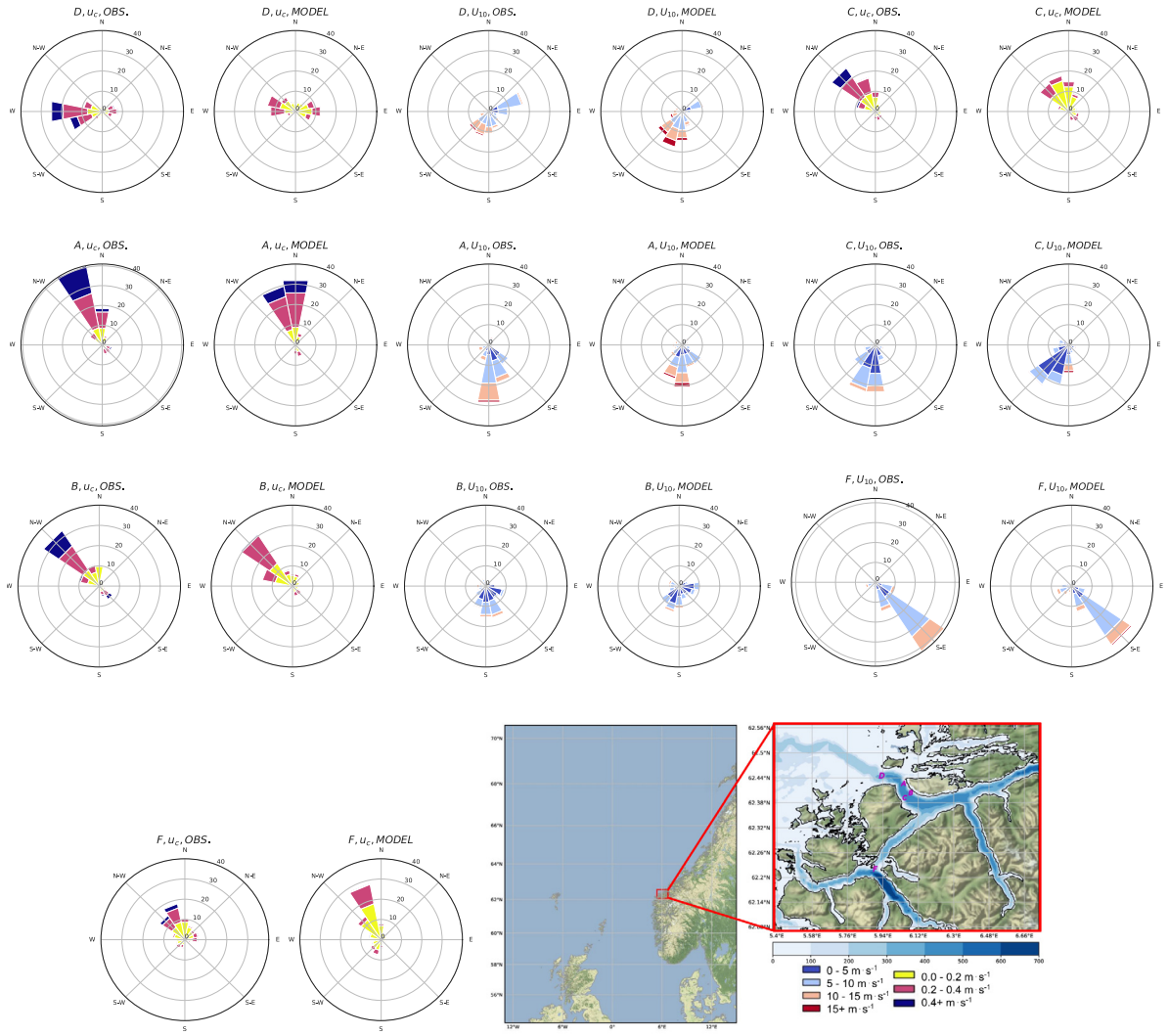

Fig. 1. The inner domain of simulations (red rectangular) with locations of wave buoys A–D and F (lower right panels). Observed (obs.) and modelled (nearest grid point of Norkyst800/WRF0.5 data as interpolated to SWAN grid) surface current (u_c) and wind (U_{10}) roses at different buoy locations during three winter periods (December 2017–February 2020). Current and wind directions follow oceanographic and meteorological convention, respectively.

2.1.2. Wave–current interactions

In the SWAN model, the wave–current interactions are mainly taken into account in the left side of Eq. (1) via the change in propagation velocities. The propagation velocities in physical and spectral space under the effect of surface currents are given by

$$(c_x, c_y) = \boldsymbol{c}_g + \boldsymbol{u}_c, \tag{5}$$

$$c_\sigma = \frac{\partial \sigma}{\partial d}\left(\frac{\partial d}{\partial t} + \boldsymbol{u}_c \cdot \nabla d\right) - c_g \boldsymbol{k} \cdot \frac{\partial \boldsymbol{u}_c}{\partial s}, \tag{6}$$

and

$$c_\theta = -\frac{1}{k}\left(\frac{\partial \sigma}{\partial d}\frac{\partial d}{\partial m} + \boldsymbol{k} \cdot \frac{\partial \boldsymbol{u}_c}{\partial m}\right). \tag{7}$$

Here s is a coordinate in the wave direction and m is perpendicular to s.

Finally, currents also affect the right-hand side of Eq. (1) through the wind input term S_{in} since the wind speed in a frame of reference moving with the currents experiences a relative wind vector (difference between wind and surface current vectors).

2.2. Model set-up and boundaries

SWAN was run in non-stationary mode with spherical coordinates, a 10-minute time step, 36 directions, and 32 discrete frequencies logarithmically spaced from 0.04 to 1 Hz. The inner domain with grid resolution 250 m × 250 m (red rectangular box in Fig. 1 (lower right panel)) is nested into the outer grid of 1 km × 1 km (more details in Christakos et al. (2020)).

2.2.1. The ocean forcing

The ocean (surface current) forcing is provided by the Norkyst800 ocean model system (Albretsen et al., 2011) with a 1-hourly temporal resolution. Norkyst800 is a high-resolution ocean modelling system that covers the whole of the Norwegian coast. The system predicts current, salinity, temperature and water level. Norkyst800 is based on the numerical ocean model ROMS (Regional Ocean Modelling System, Shchepetkin and McWilliams (2005), Haidvogel et al. (2008) with a spatial horizontal resolution of 800 m and 35 vertical levels. The surface currents are used to force the wave model, and the uppermost vertical level corresponds to a depth 10–20 cm below surface. The exact thickness depends on the total water depth, as ROMS applies a terrain-following vertical coordinate. The main external forcing

agents in Norkyst800 come from a high-resolution atmospheric model (AROME2.5 km), a hydrological runoff model, a global tidal model and a large-scale ocean model. Asplin et al. (2020) found good agreement between Norkyst800 and current observations in coastal and fjord areas, particularly in the upper 10–20 m.

2.2.2. The wind forcing

The atmospheric forcing used for the SWAN wave model runs is generated by WRF0.5, which is a dynamical downscaling of the ERA-Interim reanalysis (Dee et al., 2011) using the Advanced Research WRF-ARW (Skamarock et al., 2008) numerical weather prediction model version 3.5.0 (more details about WRF0.5 are provided by Christakos et al. 2020). The WRF0.5 wind fields in the fjord system have a spatial and temporal resolution of 0.5 km and 1 h, respectively.

2.2.3. The offshore wave boundaries

The NORA10 hindcast provided the wave conditions at the grid boundaries of the outer SWAN model domain with 3-hourly temporal resolution (information about the spectral nesting and interpolation can be found at Breivik et al. (2009)). The NORA10's wave component is a 10 km × 10 km WAM model forced by HIRLAM winds nested inside a 50 km × 50 km outer domain forced by ERA-40 winds (Reistad et al., 2011). This outer domain covers a large part of the North Atlantic, which provides realistic simulations of low-frequency wave (e.g., swell) propagation from the open sea to the Norwegian coast. The hindcast uses analysed fields from the European Centre for Medium-Range Weather Forecasts (ECMWF) as initial and boundary conditions and has been found to compare well with a similar downscaling of ERA-Interim (Haakenstad et al., 2020).

2.2.4. The wave simulations

To assess the effect of the currents on wave dynamics, we have performed two wave simulations. The first is a control run with wind forcing, hereafter SWAN, and an alternative run with wind and current forcing ($SWAN_C$). The wave simulation period includes three winters (December, January, February) from December 2017 to February 2020. In addition, we performed wave simulations for a selected case with alternative current forcings equal to 2% of the wind forcing or 120% of the Norkyst800 current speed. These simulations are denoted $SWAN_{2\%W}$ and $SWAN_{120\%C}$, respectively.

2.3. Observations

Observations from wave buoys (Fig. 1) are used to assess the performance of different model set-ups. The measurements include both integrated wave parameters and spectral wave data, as well as wind and currents (Furevik et al., 2020). The acoustic measurements of surface currents are obtained at 1 m below the sea surface. For the evaluation of model wind speed, the observed wind is adjusted to 10 m height (U_{10}) using a logarithmic profile (e.g., Christakos et al., 2020).

2.4. Statistical parameters

The statistical characteristics of the sea surface can be expressed as spectral moments as follows,

$$m_n = \int_0^\infty \sigma^n E(\sigma)\, d\sigma \qquad n = -1, 0, 1, \ldots, \tag{8}$$

where m_n is the nth-order moment of $E(\sigma)$. In this study we estimate the first positive (m_1) and negative (m_{-1}) moment. The former gives more weight to higher frequencies, while the latter gives more weight to lower frequencies. When we compare to observations, these moments were determined by integrating up to the maximum frequency of the observations.

The significant wave height is estimated from the zeroth-order moment as

$$H_{m_0} = 4\sqrt{m_0}. \tag{9}$$

The spectral bandwidth (Longuet-Higgins, 1975) is defined as

$$\nu = \sqrt{\frac{m_0 m_2}{m_1^2} - 1} = \sqrt{\left(\frac{T_{m_{01}}}{T_{m_{02}}}\right)^2 - 1}. \tag{10}$$

The directional spreading is estimated following Kuik et al. (1988) as

$$\sigma_\theta = 2\left(1 - \sqrt{\frac{(\iint \sin\theta E(\sigma,\theta) d\sigma d\theta)^2 + (\iint \cos\theta E(\sigma,\theta) d\sigma d\theta)^2}{(\iint E(\sigma,\theta) d\sigma d\theta)^2}}\right). \tag{11}$$

The average relative difference (RD) of a variable χ (e.g., H_{m_0}) is defined as

$$\overline{\mathrm{RD}_\chi} = \frac{\overline{\Delta\chi}}{\overline{\chi_{\mathrm{SWAN}}}} \tag{12}$$

where $\Delta\chi = \chi_{\mathrm{SWAN}_C} - \chi_{\mathrm{SWAN}}$ is the difference of χ between SWAN_C and SWAN.

The temporal mean of χ over the whole simulation period is denoted $\overline{\chi}$, while the mean of the highest five percentiles, $q \geq 0.95$, denoted $\overline{\chi_{q\geq 0.95}}$.

The dimensionless width of a fjord location is calculated as

$$\tilde{X}_w = \frac{g X_w}{U_{10}^2}. \tag{13}$$

Here X_w is the width (distance across the fetch, for more details see Christakos et al. 2021).

2.5. Error metrics

The error metrics used in the present study are the Pearson correlation coefficient (R) which describes how model estimates (y_i) and observations (x_i) are linearly correlated, where R^2 ranges between 0 (no correlation) and 1 (perfect linear correlation),

$$R = \frac{\sum_{i=1}^N (y_i - \bar{y})(x_i - \bar{x})}{\sqrt{\sum_{i=1}^N (y_i - \bar{y})^2}\sqrt{\sum_{i=1}^N (x_i - \bar{x})^2}} \tag{14}$$

The bias is defined as the mean difference between y_i and x_i,

$$\mathrm{Bias} = \overline{y_i - x_i} \tag{15}$$

the scatter index is defined as the standard deviation of the difference between y_i and x_i normalized by the mean of x_i

$$\mathrm{SI} = \frac{\sqrt{\frac{1}{N}\sum_{i=1}^N [(y_i - x_i) - (\bar{y} - \bar{x})]^2}}{\bar{x}}. \tag{16}$$

Finally, the normalized difference (bias) of H_{m_0} is defined as

$$\mathrm{NBI} = \frac{H_{m_{0,SWAN_{(C)}}} - H_{m_{0,obs}}}{H_{m_{0,obs}}} \tag{17}$$

Here, $H_{m_{0,SWAN_{(C)}}}$ and $H_{m_{0,obs}}$ are the modelled and observed significant wave height. For the estimation of NBI, only $H_{m_{0,SWAN_{(C)}}}$ and $H_{m_{0,obs}}$ values greater than 0.20 m are considered.

3. Results

3.1. Model evaluation

Norkyst800 reproduces the dominant current direction well (Fig. 1), with the largest deviations at locations C and F. Compared to observations, the modelled surface current speeds are weaker at all locations. The dominant wind direction is well represented, but the modelled wind speed is too strong in most parts of the fjord system, as illustrated in Fig. 1. Modelled wind and current directions are closely aligned in locations A, C and F. In location D, the current direction is both from east and west as the buoy is located in the centre of the straight, where both inflows from the west and outflow from the east occur in the

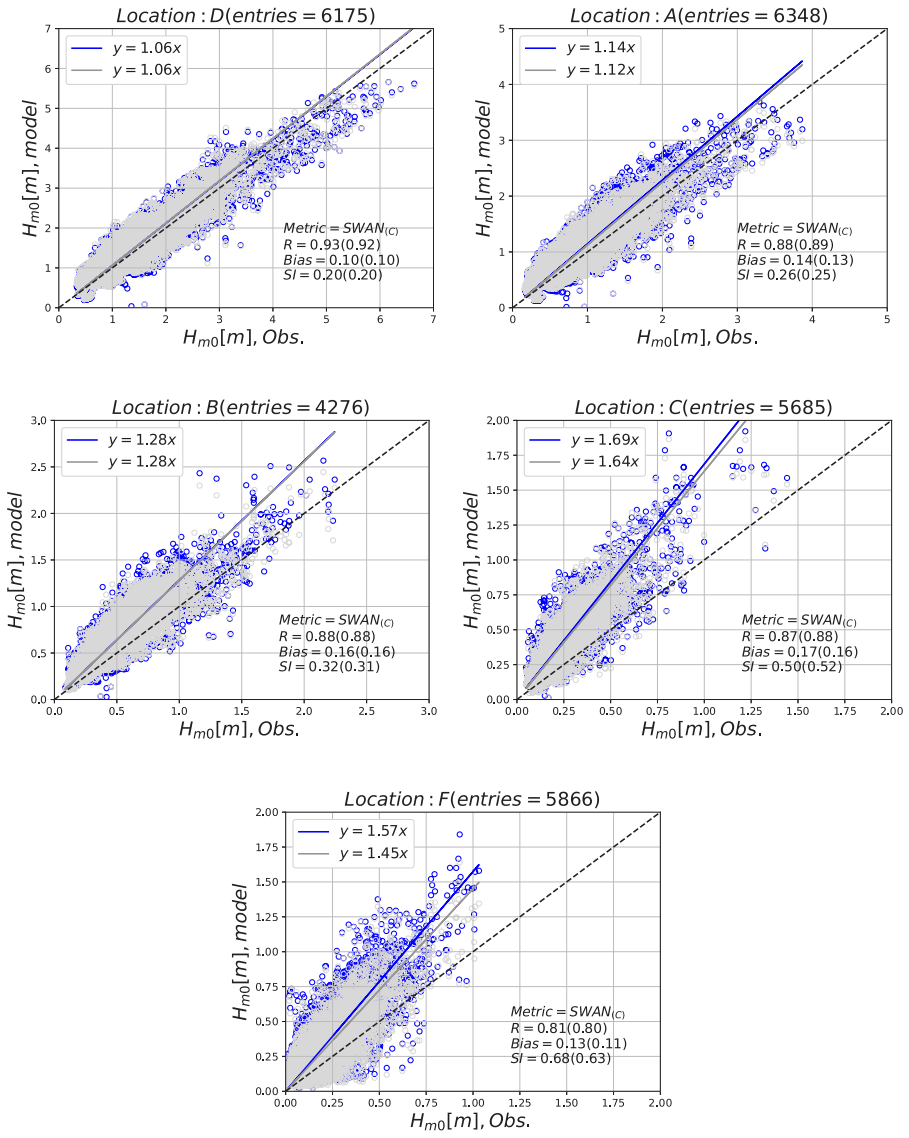

Fig. 2. Scatter plots and the corresponding $y = \frac{\bar{y}}{\bar{x}}x$ line of observed and simulated H_{m_0} for SWAN (blue) and SWAN$_C$ (grey) at different buoy locations during three winter periods (December, 2017–February, 2020).

southern and northern part of Breisundet, respectively. The dominant wind direction at D is from the southwest. In locations A and B, the main current and wind directions are from the south/southeast. At location C, the dominant current and wind directions are from the southeast and south/southwest, respectively. In the innermost location (F), the dominant directions of both current and wind are from the southeast. At all fjord locations, both wind and current directions are determined by the axis of the fjord.

The observed and modelled dominant wave directions agree at all locations (not shown). At location D, A, B, and C (Sulafjorden), the main wave direction is from the open ocean aligned with the fjord axis (northwest) (Fig. 1). This indicates (i) the dominant role of the open sea waves penetrating into Sulafjorden and (ii) the importance of fjord geometry in controlling the wave direction. At location F the dominant wave direction is from the southeast—also aligned with the fjord axis.

As seen in Fig. 2, both SWAN and SWAN$_C$ show similar overall performance (0–5 percentage points difference) at locations exposed (or partially exposed) to the open sea (D, A, B and C). The simulation with current forcing (SWAN$_C$) shows an overall better performance in terms of wave height. Both runs perform best ($R \geq 0.87$, bias ≤ 0.16 and SI ≤ 0.32) at the most exposed locations, i.e., D, A and B. In locations C, both model runs overestimate significantly (60–70%) the wave height. At the same location SWAN$_C$ shows a slightly improved R and bias, and a lower (by 5 percentage points) overestimation of observed wave heights compared to SWAN.

The highest difference between the model simulations is detected at location F, where the simulations with surface currents (SWAN$_C$) improve the wave estimates by 12 percentage points compared to SWAN. In addition SWAN$_C$ shows a reduction in SI (from 0.68 to 0.63), bias (from 0.13 to 0.11), but also a small decrease in R (from 0.81 to 0.80).

The average spectrum and the average spectral moments (m_{-1} and m_1) of the overall and the highest quantiles ($q \geq 0.95$) for SWAN, SWAN$_C$ and observations are shown in Fig. 3. Both model runs perform similarly for exposed locations (D—not shown, A and B) with SWAN$_C$ providing slightly better estimates for the spectral moments m_{-1} and m_1. Regarding the highest 5%, the wind sea part of the spectrum in A and B improves slightly when current forcing is included. The average spectrum in location C shows that both simulations have a near identical shape, while the simulated energy of the dominant waves (around the peak) and the spectral moments overestimate ca. 2–3 times the observations. Regarding the highest quantiles ($q \geq 0.95$) at C, SWAN$_C$ shows (i) slightly higher energy of the lowest frequency peak (e.g., swell) and (ii) lower energy of the wind sea part with

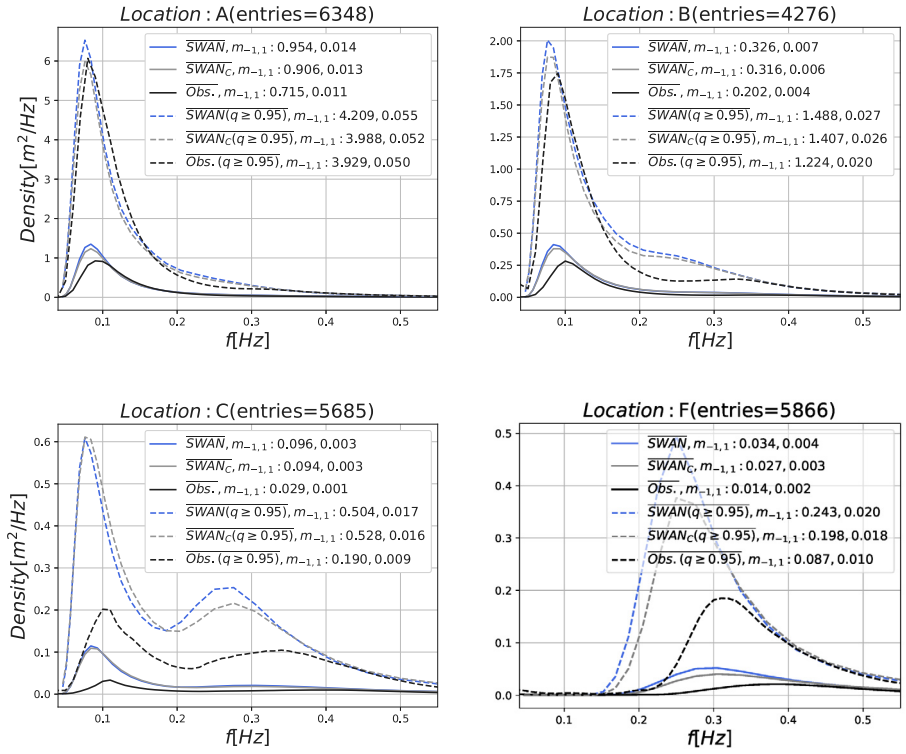

Fig. 3. The average spectra (solid) and the average of the highest 5% (dashed) of observed (black), SWAN (blue) and SWAN_C (grey) at different buoy locations during three winter periods (December 2017–February 2020).

the peak frequency being shifted to higher frequencies than SWAN. When the wave simulations are compared to observations, the high frequency density peak is estimated more accurately by SWAN_C while the low frequency density peak is overestimated by ca. 2 times in both simulations with SWAN_C.

In the most sheltered location (F), where swell is nearly absent and wind sea dominates the wave climate, we observe the highest reduction (by ca. 20% in $q \geq 0.95$) of the dominant energy when current forcing is present (SWAN_C), fitting best the observed spectra. SWAN_C also provides the best performance in terms of spectral moments for both the overall average and the highest quantiles.

3.2. Met-ocean climatology: Winter season

Based on Norkyst800 data from the winter seasons (December 2017–February 2020), we visually identify two main patterns of surface currents (Fig. 4-top): (i) along the coastline, and (ii) an outward (from inner to outer fjord locations) current with a local maximum at the inlet of Sulafjorden and at narrow inner fjords, e.g., close to location F. Both patterns have a similar magnitude, with $\overline{u_c} \approx 0.2$–$0.3$ m s^{-1} and $\overline{u_{c(q\geq 0.95)}} \approx 0.5$–$0.7$ m s^{-1}.

Similarly, the wind conditions are characterized by strong winds along the coast (from the southwest) and within the fjords, with $\overline{U_{10}}$ and $\overline{U_{10(q\geq 0.95)}}$ up to 10 m s^{-1} and 24 m s^{-1}, respectively (Fig. 4-middle). The wave climate (Fig. 4-bottom) is dominated by offshore waves from the west/northwest in areas off the fjord system ($\overline{H_{m_0}}$ and $\overline{H_{m_0(q\geq 0.95)}}$ up to 4 m s^{-1} and 8 m s^{-1}, respectively). Wave conditions at inner fjord locations are dominated by the local wind sea, with wave heights approximately 4 times lower compared to offshore waves.

3.3. Spatial current effects on fjord waves

To identify the most affected areas by the ocean currents, the average relative difference between SWAN and SWAN_C for H_{m_0}, σ_p (relative peak frequency), ν (spectral bandwidth) and the average $\cos(\Delta\theta_p)$ (θ_p: peak wave direction) over the fjord system is illustrated in Fig. 5. The $\cos(\Delta\theta_p)$ describes the magnitude of wave refraction where 1 and 0 indicate no and 90° refraction, respectively. When current forcing is included (SWAN_C), we observed (i) a reduction of wave height of up to 15% in the inner fjord locations while at the exposed locations, the change is between −2.5% and 5%, (ii) the relative frequency in the fjord locations generally increased when currents were accounted for, with the change being up to 15% (off the fjord system, the use of currents had practically no effect on the relative frequency), (iii) an increase up to 5% of the spectral bandwidth at inner fjord locations, and (iv) weak refraction at inner fjord locations and nearly no refraction off the fjord system.

Including the surface currents have no significant impact on the directional spread on average (Fig. 6, left). However, the top 5% of the currents (Fig. 6, right) are strong enough to modify the spread of the wave field in the fjord system. In the exposed areas, where the strong outward currents meeting the incoming long and energetic waves, SWAN_C shows up to 6 degrees narrower directional width (spread) than SWAN. At inner fjord locations, where surface currents and waves are generally in the same direction, $\Delta\sigma_\theta$ is positive, up to 6 degrees, indicating that the current forcing induces wider directional spread.

3.4. Inner fjord location

Focusing on an inner fjord area such as location F where the highest differences between SWAN and SWAN_C are detected, we observe that for most of the time (not shown) surface currents follow the wave direction resulting in an overall decrease of wave height. Fig. 7 reveals that SWAN_C performs better (lower NBI) than SWAN for low to moderate dimensionless width (X_w) where most of the data is observed. As it is illustrated by Christakos et al. (2021), the highest NBI at F for different source term packages is observed for low to moderate dimensionless width.

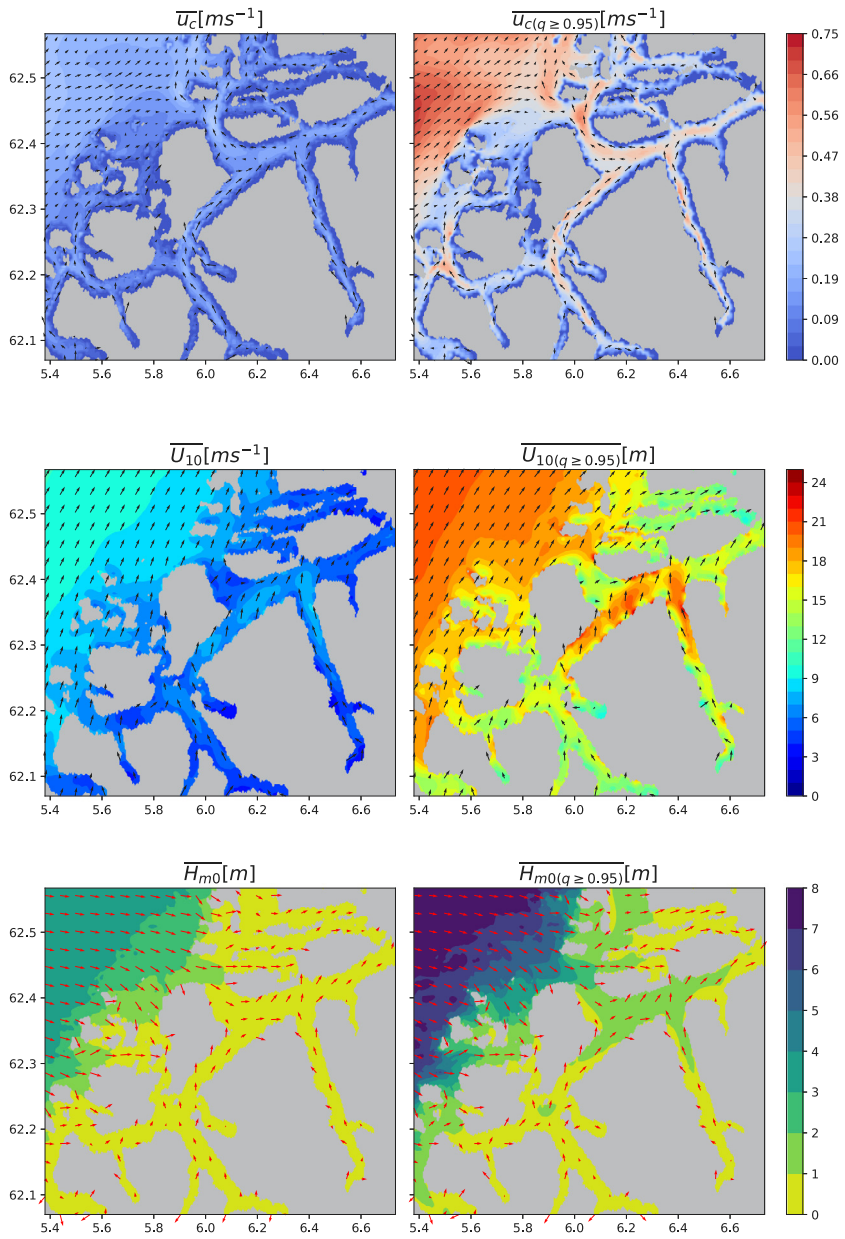

Fig. 4. Overall mean (left) and mean of the highest 5% (right) of u_c (arrows indicate the current direction), U_{10} (arrows indicate the wind direction) and H_{m_0} (arrows indicate the mean wave direction) derived from SWAN during three winters (December, 2017–February, 2020).

3.5. Case: wind sea and following currents at inner fjord location

To further understand the wave–current interactions at the most affected areas (location F), we perform a case study where strong winds and surface currents have approximately the same direction. More specific, on January 15, 2018, strong winds ($\geq$ 15 m s^{-1}) from the southeast generated a high local wind sea (Christakos et al., 2020) at the inner fjords (location F). Figs. 8 (top-right panels) and 10 (top-left panel) reveal strong surface currents aligned with the inner fjords axis at January 15, 2018, 9 UTC.

Time series of wind, surface currents and integrated wave parameters at location F during the event are presented in Fig. 8 (top). Both speed and direction of the surface current and wind are in good agreement with observations. Small differences are detected between $\text{SWAN}_{2\%\text{W}}$, SWAN_{C} (Norkyst800) and observations for both surface current velocity and direction. The observed mean wave direction (θ) ranges from 130° to 150° (not shown). All simulations predict the wave direction well. The modelled surface current direction θ_c is in good agreement with observations. Because of a weak wave refraction induced by the currents, the difference in wave direction between SWAN and SWAN_{C} is below 10°. The observed H_{m_0} reaches up to ca. 1 m. The simulations without current forcing strongly overestimated H_{m_0}, but this overestimation is sharply reduced in the simulation forced with the wave-following currents. Similar results are also detected in f_p (peak frequency).

Furthermore, the observed/modelled current profile (Fig. 9) indicates the existence of a stratified water column with two layers: (i) an outward surface current and (ii) an inward current at ca. 50–60 m depth. The outward surface current is a wind-driven current.

The sharp reduction of wave energy due to the following currents is illustrated in Fig. 8 (bottom). The energy of observed dominant waves is ca. 50% lower compared to simulations without current forcing. SWAN simulations also under-predict the peak frequency. Including the current forcing improves the estimation of dominant wave energy and peak frequency. The energy of the spectral tail above ca. 0.35 Hz is modelled similarly in all simulations, being somewhat higher compared

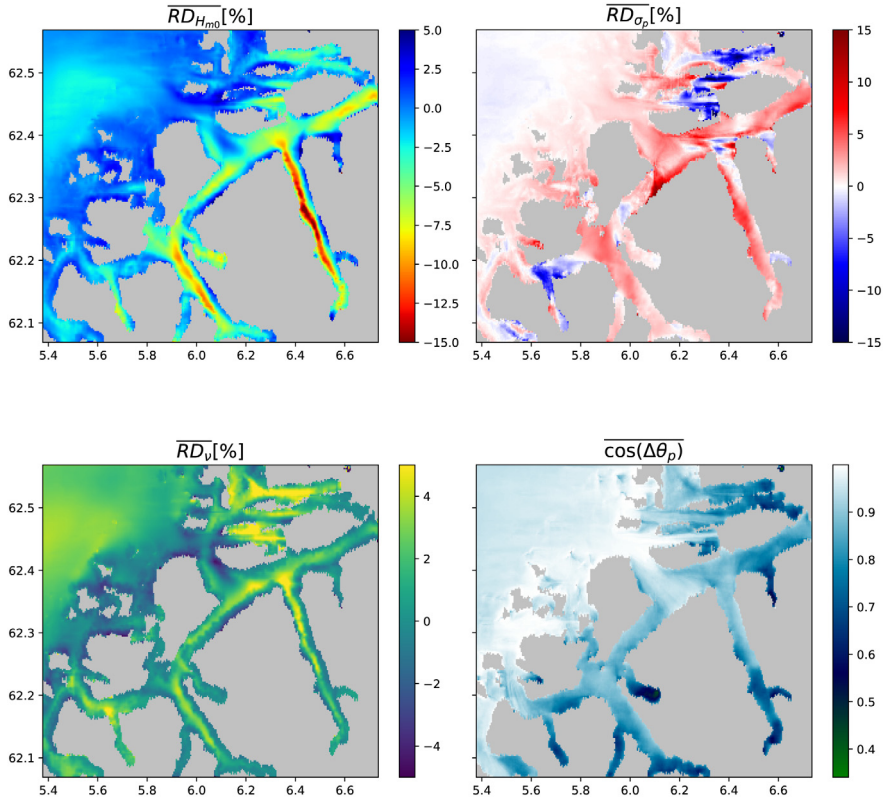

Fig. 5. Average relative difference (RD) between SWAN_C and SWAN for significant wave height (H_{m0}), relative peak frequency (σ_p) and spectral bandwidth (ν) and average $\cos(\Delta\theta_p)$ for three winter periods (December, 2017–February, 2020) over the fjord system.

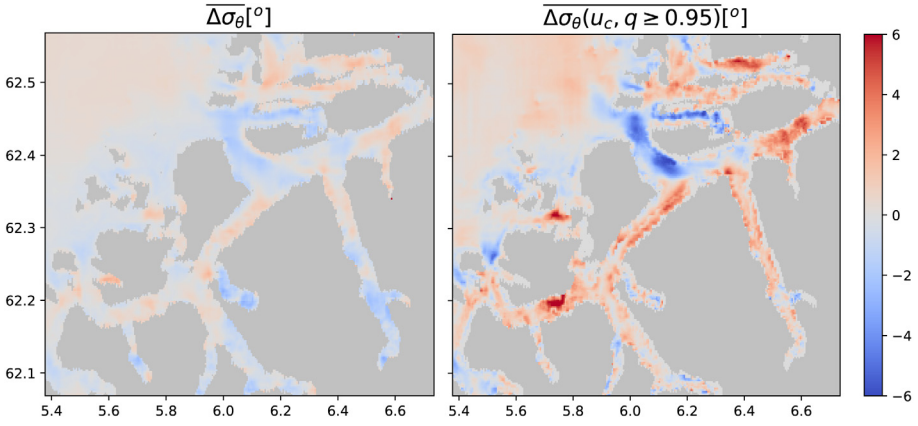

Fig. 6. Overall average directional spread $\Delta\sigma_\theta$ (left) and average $\Delta\sigma_\theta$ for the strongest 5% of the current speed u_c (right).

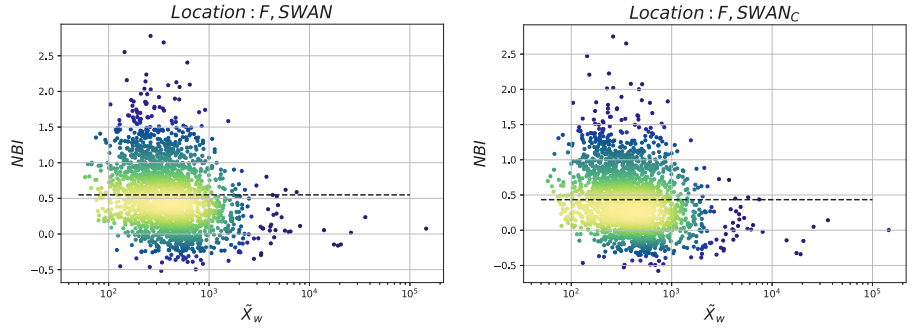

Fig. 7. Dimensionless width, $\tilde{X}_w$, as a function of the normalized bias, NBI, at location F (only for $H_{m0,SWAN_{(C)}\&obs.} > 0.2$ m) for SWAN (left) and $SWAN_C$ (right). Dark blue colour represents low density (number of overlapping points) while light yellow represents high density. The dashed line shows the $\overline{NBI}$ (overall mean of NBI).

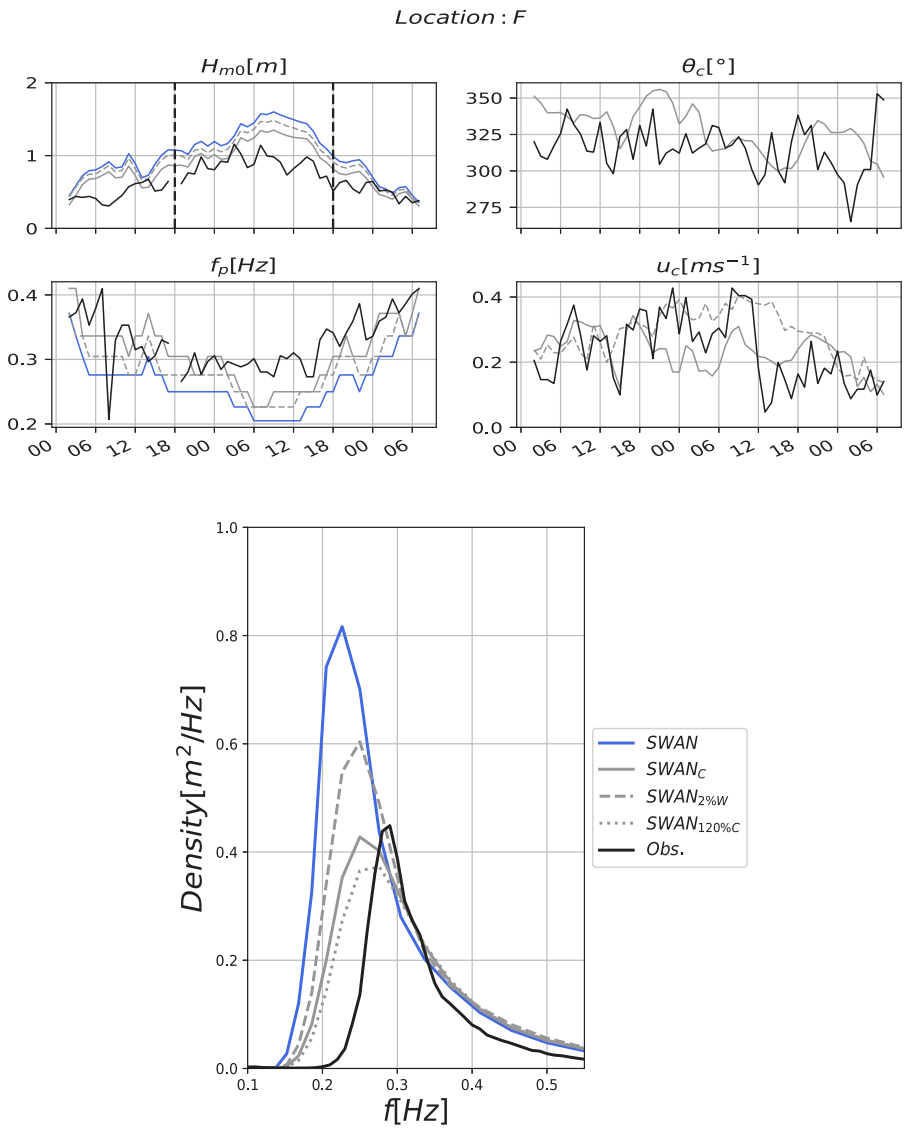

Fig. 8. Top panels: time series of H_{m_0}, θ_c (surface current direction), f_p and u_c (surface current speed) for modelled and observed data at location F during January 14, 2018, at 02 UTC to January 16, 2018, at 08 UTC. Lower panel: average density, as a function of absolute frequency, during time period illustrated with vertical dashed lines at the top-left panel (H_{m_0}).

to the observations. Using the alternative current forcing ($SWAN_{2\%W}$) also provides a better estimation of dominant wave energy compared to SWAN, reducing the peak density by 27%. Increasing the surface current of Norkyst800 by 20% ($SWAN_{120\%C}$), we observe a reduction of energy of the dominant waves by ca. 12% compared to $SWAN_C$.

The spatial difference in H_{m_0} between simulations with and without current forcing and the modelled surface current are presented in Fig. 10 (top) on January 15, 2018, at 09 UTC. The highest negative value (up to −0.4 m) is detected at the cross-section of the fjords close to location F, where $u_c > 0.3$ m s^{-1}. No significant differences in the wave direction are detected between the two simulations. In addition, the current forcing reduces the relative peak wave period by up to 0.6 s for most of the fjord area near F (not shown).

A snapshot of the deep water source terms, S_{in}, S_{ds} and S_{nl4}, over the fjord cross-section at location F at January 15, 2018, at 09 UTC is shown in Fig. 10 (bottom). The results indicate that the source terms are significantly affected by the presence of surface currents. More specific, the $SWAN_C$ shows reduced magnitudes by ca. 30% in the deep water source terms, for the dominant waves, and ca. 14% higher σ_p compared to SWAN. For shorter waves (relative frequency greater than 0.25 Hz), both simulations show minor differences for S_{in} and S_{ds}.

4. Discussion

SWAN (without current forcing) provides a good overall model performance in terms of H_{m_0} and average spectral characteristics in exposed locations where mixed wind sea-swell conditions are observed, with minor differences compared to $SWAN_C$ (with the current forcing). In addition, accounting for currents have a positive effect on the accuracy of the local wind sea part of the spectrum in these locations. The wave climate in the exposed areas to the open sea is dominated by strong swell or/and old wind sea from west/northwest (Fig. 4). On the other hand, the surface current (and wind) off the fjord system has a dominant direction from the southwest which is near perpendicular to wave direction leading to:

(i) a weak Doppler shift since $\boldsymbol{k} \cdot \boldsymbol{u_c} \longrightarrow 0$,

(ii) a weak change in σ due to no significant changes of current field along the same direction ($c_g \boldsymbol{k} \cdot \frac{\partial \boldsymbol{u_c}}{\partial s} \longrightarrow 0$),

(iii) a weak current-induced refraction while there are no significant changes of current field across the wave crest ($\boldsymbol{k} \cdot \frac{\partial \boldsymbol{u_c}}{\partial m} \longrightarrow 0$).

(iv) a weak modulation of the dominant waves due to no significant changes in group velocities because the surface current velocities are much lower than the typical swell group velocity. For example, a wave with a period of 14 s ($c_g \approx 11$ m s^{-1} for deep water) under the effect of surface currents of 0.7 m s^{-1} experiences ca. 6% change of absolute group velocity.

As it was also concluded by Christakos et al. (2020), simulations with pure wave propagation (without wind forcing) showed quite similar overall results in the exposed fjord locations, revealing the dominant role of boundary (offshore) waves. Therefore, in the exposed locations, the ocean forcing has a secondary role after the quality of boundary waves and wind forcing.

In contrast to exposed locations, SWAN performs quite poorly at inner locations. In these areas both the current (Section 3) and the wind forcing (Christakos et al., 2020) are essential for more accurate wave estimates. More specifically, the surface currents and the wind generated waves are nearly aligned (following) leading to:

(i) a maximum Doppler shift since $\frac{\boldsymbol{k}\cdot\boldsymbol{u}_c}{|\boldsymbol{k}||\boldsymbol{u}_c|} \longrightarrow 1$,

(ii) a change of σ due to changes of the current along the wave direction ($-c_g\boldsymbol{k}\frac{\partial \boldsymbol{u}_c}{\partial s}$). The following currents induce a negative $-c_g\boldsymbol{k}\frac{\partial \boldsymbol{u}_c}{\partial s}$ leading to a reduction of σ (Eq. (6)). However, energy stretching and a reduced relative wind by the following currents resulted in a higher σ_p.

(iii) a weak current induced refraction due to some variation of current fields across the wave crest ($\boldsymbol{k}\frac{\partial \boldsymbol{u}_c}{\partial m}$),

(iv) a strong modulation of the dominant waves due to significant changes on group velocities; considering that the surface current velocities at inner fjord is about 0.5 m s^{-1}, a typical wave period of young wind sea of 3.5 s with velocity equal to 2.7 m s^{-1}, which corresponds to ca. 18.5% increase of absolute group velocity,

(v) a ca. 3% reduction of wind speed due to the relative wind effect; considering a case with relative high wind speed U_{10} of about 15 m s^{-1} and u_c of ca. 0.5 m s^{-1} the relative wind speed is about 3% lower than U_{10},

(vi) since the wind input (Eq. (4)) is a function of inverse wave age ($\frac{u_*}{c}$ or $\frac{u_*\sigma}{g}$ for deep water), changes in both σ and u_* should also be taken into account. In case of a following current and a divergent current field, the inverse wave age is decreased since both u_* (relative wind effect) and σ ($-c_g\boldsymbol{k}\cdot\frac{\partial \boldsymbol{u}_c}{\partial s} < 0$ in Eq. (6)) are decreased.

The main problem at inner fjord locations is the overestimation of wave energy by the model. Adding the current forcing reduces the dominant wave energy's estimation by ca. 50% when using the WESTH physics package (Fig. 8). A reduction of similar magnitude is also seen with the other source terms packages (not shown). This 50% reduction is also in the same order magnitude as changing the source term package from ST6 (Babanin et al., 2010) to WESTH when not accounting for the currents (Christakos et al., 2021). A common engineering approach to achieve more precise wave estimations is the calibration of the wave model. For instance, tuning the white-capping coefficient (C_{ds}) is widely used when under/over-prediction of wave energy is observed (e.g., Amarouche et al., 2019). However, at inner fjord locations, ignoring the ocean forcing can lead to an over-calibration of the wave model.

As a rule of thumb, the surface current induced by wind is about a few percent of the wind (e.g., 2%) at open ocean (e.g., Fergestad et al., 2019). For instance, wind speed of 15 m s^{-1} should induce a fully developed wind-driven current of 0.3 m s^{-1}. Our sensitivity study

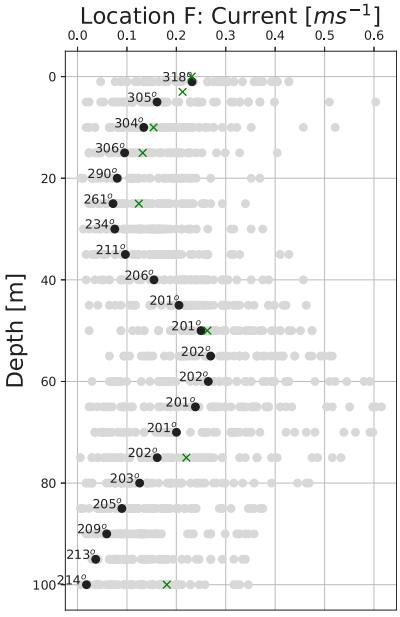

Fig. 9. Observed (grey for 10-min values and black for average speed and direction in oceanographic convention) and modelled ('x' for average values) ocean current in different depths for period January 14, 2018, at 02 UTC to January 16, 2018, at 08 UTC.

indicates that for location F, where the currents are restricted by the narrow fjord geometry, this simple practice used in SWAN$_{2\%W}$ can outperform SWAN with no current forcing. However, SWAN$_{2\%W}$ is not as accurate as SWAN$_C$, where the actual current forcing is used.

The ocean current in spectral waves models (e.g., SWAN), is usually taken as a surface or depth-uniform current and applied homogeneously to all wave components. However, ocean currents are often vertically sheared to some extent. In this case, surface waves are not affected only by the current at the surface, but rather by a depth-weighted current (Eq. (18) in Kirby and Chen (1989)). Short (kd $\gg$ 1) and long (e.g., swell, kd $\ll$ 1) surface waves are affected differently: the former mostly feel the surface current, while the latter are also affected by below-surface currents, which are typically not as strong. In some areas, such as in the mouth of the Columbia River, the current variation with depth has been shown to be important for accurate surface wave predictions (Zippel and Thomson, 2017). In a sheltered fjord area (location F), where the highest impact of currents on waves is observed, we found approximately 5% difference (not shown) between the surface and the depth-weighted current (based on the average modelled current profile of Fig. 9) for the dominant waves (0.2–0.3 Hz). Since the effect of currents is weak at the exposed locations, a more elaborate method to estimate the current forcing is not warranted. Therefore, using the surface current is a reasonable approach over our entire study area.

The presence of currents influences the spectral bandwidth in sheltered inner fjord locations. By including current forcing, the spectral bandwidth is increased (broader spectrum) by up to 5% at the majority of the inner locations. This is consistent with a reduced wind input because of a lower relative wind speed, a wave field in a later stage of the development, and energy stretching due to the following current. Similarly, the directional spreading is also affected by the presence of currents, with the maximum differences being observed during the highest surface currents. In Sulafjorden (a fjord exposed to the open ocean), the opposing currents (to long incoming waves, e.g., swell) result in energy bunching and a decrease of σ_θ, while the following currents within the inner fjords lead to energy stretching and increase of σ_θ.

In Sulafjorden, location C is the one most sheltered from incoming long waves. Both model simulations show a strong overestimation of

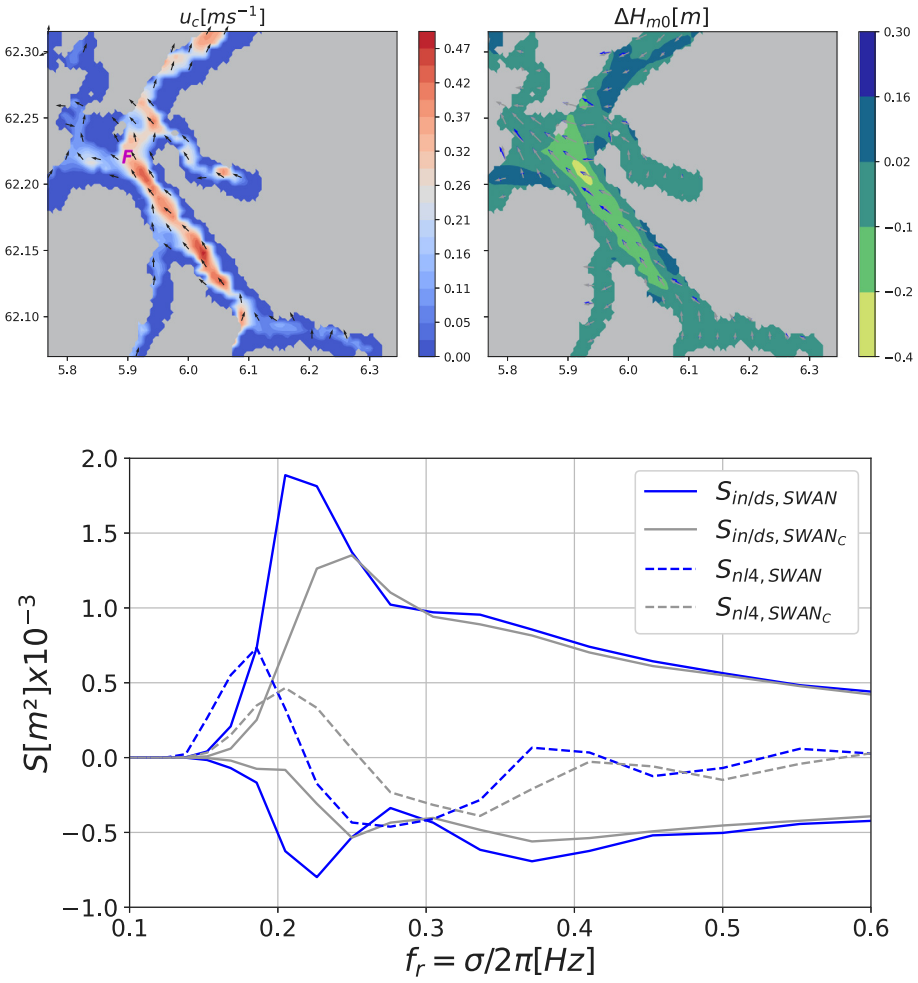

Fig. 10. Snapshot of January 15, 2018 at 09 UTC when the modelled wind speed, U_{10}, at location F was ca. 20 m s^{-1} from southeast. Top panels show the current speed, u_c (arrows indicate the current direction), and a consequent change in significant wave height, ΔH_{m_0} (blue and grey arrows represent the peak wave direction in SWAN and SWAN$_C$, respectively). The lower panel shows the deep water source terms S_{in}, S_{ds} and S_{nl4} at location F .

the overall wave energy. By including current forcing, we observed a slight degradation for low frequency waves (m_{-1}) during the highest 5% cases. This can be explained by the presence of opposing currents to incoming long waves (the swell which dominates the wave climate of the open ocean, see Semedo et al. 2014) that leads to energy bunching and consequently to overestimation of the low frequency wave energy. Christakos et al. (2020) showed that increasing the spatial grid resolution improves the results in partly sheltered locations such as C, we thus believe that a finer grid (<250 m) may improve the model performance during long wave propagation at C.

As presented by Christakos et al. (2021), the highest NBI at location F for the different source term packages tested is found for low to moderate dimensionless width. Our results indicate that including current forcing improves the results, slightly reducing the NBI for low to moderate dimensionless width. However, the improvement is limited, and other factors such as the quality of wind forcing and white-capping/wind input formulations may also play a role.

The horizontal resolution of Norkyst800 is considered quite good, and in general the model topography is capable of capturing the main current features and providing reliable estimates of the surface current field in the fjord system. However, even higher resolution is the most obvious way to improve topographically induced currents in narrow fjords.

Our results demonstrate that there is a clear need for more knowledge of wave–current interactions and a more realistic description of the surface waves in nearshore areas. In this context, it is necessary to further develop our advanced numerical prediction systems via a fully coupled ocean-wave-atmosphere system, taking into account the ocean and atmosphere as a unified system.

Finally, the presented results can be useful to other fjord systems with similar characteristics, i.e., narrow and deep topography, strong stratification and weak bathymetry effects, which are typical for most of the fjords around the world (e.g., Norway, the Faroe Islands, Iceland, Greenland, New Zealand and Chile). In addition, our results might offer some transferable insights to larger narrow enclosed or semi-enclosed water bodies such as the Gulf of Finland or Lake Ontario, where oceanic swell is absent. In larger basins, however, the surface current can be more complex (Westerlund et al., 2019) and a possible wind-wave misalignment caused by slanting fetch (Donelan et al., 1985; Pettersson et al., 2010) might weaken the effects of the currents. Our results are not expected to carry over to exposed shallow shorelines, where bathymetry plays a key role.

5. Summary and conclusions

Wave modelling in complex fjord systems has not received much attention earlier due to lack of observations and the need for very high-resolution atmosphere, wave and ocean models. We have investigated the performance of the saturation-based white-capping parameterization in the SWAN model in the presence of currents. Including current forcing in wave model integration improved the wave field in most locations investigated. All locations show improved results of the wind

sea part of the spectrum. At inner (sheltered) fjord locations, the inclusion of surface currents shows the largest improvement on the wave height estimates with improvements exceeding 10 percentage points. In these locations, the change in the dominant waves' group velocity is of the order of 20% due to currents, whereas in outer, more exposed, locations the change is only a third of that. Furthermore, current forcing based on 2% of modelled wind shows improved results at inner locations and can be used potentially for some cases where the actual current simulations are not available. A strong change in wave frequency σ_p, up to 10 – 15% at most of the inner fjord locations, is also observed when current forcing is included. The deep water source terms are affected by the presence of currents in the same order of magnitude. A consequence of not applying ocean forcing on fjord wave modelling can be an over-calibration of the wave model. Finally, the results indicate that the improvement in model performance is worth the added complexity of using the offline coupled model system for producing operational coastal and fjord wave simulations.

CRediT authorship contribution statement

Konstantinos Christakos: Conceptualization, Visualization, Methodology, Software, Formal analysis, Investigation, Data curation, Writing – original draft, Writing – review & editing. **Jan-Victor Björkqvist:** Methodology, Investigation, Writing – review & editing. **Øyvind Breivik:** Supervision, Writing - review & editing. **Laura Tuomi:** Supervision, Writing – review & editing. **Birgitte R. Furevik:** Supervision, Writing – review & editing, Project administration. **Jon Albretsen:** Writing – review & editing.

Declaration of competing interest

The authors declare that they have no known competing financial interests or personal relationships that could have appeared to influence the work reported in this paper.

Acknowledgements

We would like to thank the reviewers for their constructive comments that helped in improving the study. Furthermore, we would like to thank Victor Alari (Tallinn University of Technology) for fruitful discussions during the conceptualization of this article. The Norwegian Public Roads Administration funded the study under the Coastal Highway Route E39 project. We are grateful to Øyvind Byrkjedal (Kjeller Vindteknikk AS) who provided the wind forcing data. Wind and wave measurements were available via the Thredds Service at the Norwegian Meteorological Institute, https://thredds.met.no. The bathymetry data was provided by EMODnet Bathymetry Consortium (2018).

References

Albretsen, J., Sperrevik, A.K., Staalstrøm, A., Sandvik, A.D., Vikebø, F., Asplin, L., 2011. NorKyst-800 Report (1) User Manual and Technical Descriptions. Tech. Rep., Institute of Marine Research.

Alves, J.H.G.M, Banner, M.L., 2003. Performance of a saturation-based dissipation-rate source term in modeling the fetch-limited evolution of wind waves. J. Phys. Oceanogr. 33 (6), 1274–1298.

Amarouche, K., Akpinar, A., Bachari, N.E.I., Çakmak, R., Houma, F., 2019. Evaluation of a high-resolution wave hindcast model SWAN for the West Mediterranean basin. Appl. Ocean Res. 84, 225–241.

Ardhuin, F., Gille, S.T., Menemenlis, D., Rocha, C.B., Rascle, N., Chapron, B., Gula, J., Molemaker, J., 2017. Small-scale open ocean currents have large effects on wind wave heights. J. Geophys. Res. Oceans 122 (6), 4500–4517.

Ardhuin, F., Roland, A., Dumas, F., Bennis, A.C., Sentchev, A., Forget, P., Wolf, J., Girard, F., Osuna, P., Benoit, M., 2012. Numerical wave modeling in conditions with strong currents: Dissipation, refraction, and relative wind. J. Phys. Oceanogr. 42 (12), 2101–2120.

Asplin, L., Albretsen, J., Johnsen, I.A., Sandvik, A.D., 2020. The hydrodynamic foundation for salmon lice dispersion modeling along the Norwegian coast. Ocean Dyn. 70, 1151–1167.

Babanin, A.V., Tsagareli, K.N., Young, I.R., Walker, D.J., 2010. Numerical investigation of spectral evolution of wind waves. Part II: Dissipation term and evolution tests. J. Phys. Oceanogr. 40 (4), 667–683.

Booij, N., Ris, R.C., Holthuijsen, L.H., 1999. A third-generation wave model for coastal regions: 1. Model description and validation. J. Geophys. Res. 104 (C4), 7649–7666.

Breivik, Ø., Gusdal, Y., Furevik, B.R., Aarnes, O.J., Reistad, M., 2009. Nearshore wave forecasting and hindcasting by dynamical and statistical downscaling. J. Mar. Syst. 78, S235–S243.

Christakos, K., Björkqvist, J.-V., Tuomi, L., Furevik, B.R., Breivik, Ø., 2021. Modelling wave growth in narrow fetch geometries: The white-capping and wind input formulations. Ocean Model. 101730.

Christakos, K., Furevik, B.R., Aarnes, O.J., Breivik, Ø., Tuomi, L., Byrkjedal, Ø., 2020. The importance of wind forcing in fjord wave modelling. Ocean Dyn. 70 (1), 57–75. http://dx.doi.org/10.1007/s10236-019-01323-w.

Dee, D., Rosnay, P.d., Uppala, Simmons, Berrisford, Poli, P., Kobayashi, S., Andrae, U., Balmaseda, M., Balsamo, G., Bauer, Bechtold, Beljaars, de Berg, V., Bidlot, J., Bormann, N., Delsol, Dragani, R., Fuentes, M., Vitart, F., 2011. The ERA-Interim reanalysis: Configuration and performance of the data assimilation system. Q. J. R. Meteorol. Soc. 137, 553–597.

Donelan, M.A., Hamilton, J., Hui, W.H., Stewart, R.W., 1985. Directional spectra of wind-generated ocean waves. Philos. Trans. R. Soc. Lond. Ser. A Math. Phys. Sci. 315 (1534), 509–562. http://dx.doi.org/10.1098/rsta.1985.0054.

Fergestad, D., Økland, O., Stefanakos, C., Stansberg, C.T., Croonenborghs, E., Eliassen, L., Eidnes, G., 2019. LFCS Review Report - Environmental Conditions. Wind, Wave and Current in Coastal Areas. Tech. Rep., SINTEF Ocean AS, URL http://hdl.handle.net/11250/2600265.

Furevik, B.R., 2017. Kystnaere bølgevarsler på barentswatch og yr. Tech. Rep., Meteorologisk institutt.

Furevik, B.R., Lønseth, L., Borg, A.L., Neshaug, V., Gausen, M., 2020. Oceanographic observations for the Coastal Highway E39 project in Mid-Norway. URL https://thredds.met.no/thredds/catalog/obs/mast-svv-e39/catalog.html.

Garvine, R.W., 1995. A dynamical system for classifying buoyant coastal discharges. Cont. Shelf Res. 15 (13), 1585–1596.

Haakenstad, H., Breivik, Ø., Reistad, M., Aarnes, O.J., 2020. NORA10EI: A revised regional atmosphere-wave hindcast for the North Sea, the Norwegian Sea and the Barents Sea. Int. J. Climatol. http://dx.doi.org/10.1002/joc.6458.

Haidvogel, D.B., Arango, H., Budgell, W.P., Cornuelle, B.D., Curchitser, E., Lorenzo, E.Di., Fennel, K., Geyer, W.R., Hermann, A.J., Lanerolle, L., Levin, J., McWilliams, J.C., Miller, A.J., Moore, A.M., Powell, T.M., Shchepetkin, A.F., Sherwood, C.R., Signell, R.P., Warner, J.C., Wilkin, J., 2008. Ocean forecasting in terrain-following coordinates: Formulation and skill assessment of the regional ocean modeling system. J. Comput. Phys. 227 (7), 3595–3624.

Hwang, P.A., 2005. Altimeter measurements of wind and wave modulation by the Kuroshio in the Yellow and East China Seas. J. Oceanogr. 61 (5), 987–993.

Irvine, D.E., Tilley, D.G., 1988. Ocean wave directional spectra and wave–current interaction in the Agulhas from the shuttle imaging radar-B synthetic aperture radar. J. Geophys. Res. Oceans 93 (C12), 15389–15401.

Kirby, J.T., Chen, T.M., 1989. Surface waves on vertically sheared flows: approximate dispersion relations. J. Geophys. Res. 94 (C1).

Komen, G.J., Hasselmann, S., Hasselmann, K., 1984. On the existence of a fully developed wind-sea spectrum. J. Phys. Oceanogr. 14 (8), 1271–1285.

Kuik, A.J., van Vledder, G.P., Holthuijsen, L.H., 1988. A method for the routine analysis of pitch-and-roll buoy wave data. J. Phys. Oceanogr. 18 (7), 1020–1034, URL https://journals.ametsoc.org/view/journals/phoc/18/7/1520-0485_1988_018_1020_amftra_2_0_co_2.xml.

Longuet-Higgins, M.S., 1975. On the joint distribution of the periods and amplitudes of sea waves. J. Geophys. Res. (1896-1977) 80 (18), 2688–2694. http://dx.doi.org/10.1029/JC080i018p02688.

Mapp, G.R., Welch, C.S., Munday, J.C., 1985. Wave refraction by warm core rings. J. Geophys. Res. 90 (C4), 7153.

Marechal, G., Ardhuin, F., 2021. Surface currents and significant wave height gradients: matching numerical models and high-resolution altimeter wave heights in the Agulhas current region. J. Geophys. Res. Oceans.

Massey, T.C., Anderson, M.E., Smith, J.M., Gomez, J., Jones, R., 2011. STWAVE: Steady-State Spectral Wave Model User's Manual for STWAVE, Version 6.0. Tech. Rep., US Army Corps of Engineers.

Melville, K., Romero, L., Kleiss, J., 2005. Extreme wave events in the Gulf of Tehuantepec. In: Rogue Waves: Proc. 14th 'Aha Huliko 'a Hawaiian Winter Workshop, pp. 23–28.

Onorato, M., Proment, D., Toffoli, A., 2011. Triggering rogue waves in opposing currents. Phys. Rev. Lett. 107 (18).

Pettersson, H., Kahma, K.K., Tuomi, L., 2010. Wave directions in a narrow bay. J. Phys. Oceanogr. 40 (1), 155–169, URL https://journals.ametsoc.org/view/journals/phoc/40/1/2009jpo4220.1.xml.

Plant, W.J., 1982. A relationship between wind stress and wave slope. J. Geophys. Res. Oceans 87 (C3), 1961–1967. http://dx.doi.org/10.1029/JC087iC03p01961.

Reistad, M., Breivik, Ø., Haakenstad, H., Aarnes, O.J., Furevik, B.R., Bidlot, J.-R., 2011. A high-resolution hindcast of wind and waves for the North Sea, The Norwegian Sea, and the Barents Sea. J. Geophys. Res.: Oceans 116 (C5).

Ris, R.C., Holthuijsen, L.H., Booij, N., 1999. A third-generation wave model for coastal regions: 2. Verification. J. Geophys. Res. Oceans 104 (C4), 7667–7681.

Romero, L., Hypolite, D., McWilliams, J.C., 2020. Submesoscale current effects on surface waves. Ocean Model. 153.

Romero, L., Lenain, L., Melville, W.K., 2017. Observations of surface wave–current interaction. J. Phys. Oceanogr. 47 (3), 615–632.

Saetre, R., 2007. The Norwegian Coastal Current—Oceanography and Climate. Tapir Academic Press, Trondheim.

Semedo, A., Vettor, R., Ø, Breivik., Sterl, A., Reistad, M., Lima, D., 2014. The wind sea and swell waves climate in the Nordic seas. Ocean Dyn. 65.

Shchepetkin, A.F., McWilliams, J.C., 2005. The regional oceanic modeling system (ROMS): A split-explicit, free-surface, topography-following-coordinate oceanic model. Ocean Model. 9 (4), 347–404.

Skagseth, O., Drinkwater, K.F., Terrile, E., 2011. Wind-and buoyancy-induced transport of the Norwegian Coastal Current in the Barents Sea. J. Geophys. Res. Oceans 116 (8).

Skamarock, W.C., Klemp, J.B., Dudhia, J., Gill, D.O., Barker, M., Duda, K.G., Huang, X.Y., Wang, W., Powers, J.G., 2008. A Description of the Advanced Research WRF Version 3. Tech. Rep., National Center for Atmospheric Research.

SWAN team, 2017. Scientific and Technical Documentation SWAN Cycle III Version 41.20.

The Wamdi Group, 1988. The WAM model - A third generation ocean wave prediction model. J. Phys. Oceanogr. 18 (12), 1775–1810.

Toffoli, A., Waseda, T., Houtani, H., Cavaleri, L., Greaves, D., Onorato, M., 2015. Rogue waves in opposing currents: An experimental study on deterministic and stochastic wave trains. J. Fluid Mech. 769, 277–297.

van der Westhuysen, A.J., Zijlema, M., Battjes, J.A., 2007. Nonlinear saturation-based whitecapping dissipation in SWAN for deep and shallow water. Coast. Eng. vol. 54 (2), 151–170, URL http://www.sciencedirect.com/science/article/pii/S037838390600127X.

Westerlund, A., Tuomi, L., Alenius, P., Myrberg, K., Miettunen, E., Vankevich, R.E., Hordoir, R., 2019. Circulation patterns in the gulf of Finland from daily to seasonal timescales. Tellus A 71 (1).

Yan, L., 1987. An Improved Wind Input Source Term for Third Generation Ocean Wave Modelling. Rep. No. 87-8, Royal Dutch Meteor. Inst.

Zijlema, M., van Vledder, G.P., Holthuijsen, L.H., 2012. Bottom friction and wind drag for wave models. Coast. Eng. 65, 19–26.

Zippel, S., Thomson, J., 2017. Surface wave breaking over sheared currents: Observations from the Mouth of the Columbia River. J. Geophys. Res. Oceans 122 (4), 3311–3328.